Nuclear Physics A539 (1992) 112–136
North-Holland

NUCLEAR
PHYSICS A

High-spin states in ^{163}Lu

W. Schmitz, C.X. Yang*, H. Hübel, A.P. Byrne**, R. Müsseler and N. Singh***
Institut für Strahlen- und Kernphysik, Universität Bonn, Nussallee 14-16, D-5300 Bonn, Germany

K.H. Maier and A. Kuhnert****
Hahn-Meitner-Institut für Kernforschung, Glienicker Strasse, 100, D-1000 Berlin, Germany

R. Wyss
Joint Institute for Heavy-Ion Research, Oak Ridge, TN 37831, USA

Received 1 August 1991
(Revised 11 September 1991)

Abstract: High-spin states in ^{163}Lu were investigated by in-beam γ-ray spectroscopy using the multi-detector array OSIRIS. One decoupled and two strongly coupled bands were observed up to high spins and a fragment of a second decoupled band was established. The band structures are connected to previously known low-spin states. An anomalously low-frequency second band crossing is observed in one of the strongly coupled bands. Band crossing frequencies and aligned angular momenta are interpreted within the framework of the cranked shell model. $B(M1)/B(E2)$ ratios are determined and compared to calculated values. Evidence is presented that the decoupled band may have a much larger deformation than the coupled bands. We suggest that it is built on the proton $i_{13/2}$ intruder configuration.

E | NUCLEAR REACTIONS ^{130}La(^{28}Si, 4n), $E = 150$ MeV, measured $\gamma\gamma$ coincidences, $\gamma\gamma(\theta)$, ^{163}Lu deduced levels, J, cranked shell model and total routhian surface calculations.

1. Introduction

The odd-Z isotopes in the rare earth and heavier-mass region can provide rich information on several aspects of nuclear structure. Experimentally, rotational bands built on many different proton excitations have been populated up to very high spins [1-17]). Since the majority of the proton states have low to medium single-particle angular momenta j which are not so easily alignable as their high-j single-neutron counterparts in odd-N nuclei, an abundance of strongly coupled bands occurs with competing M1/E2 $\Delta I = 1$ and E2 $\Delta I = 2$ transitions. Their transition rates depend

* Permanent address: Institute of Atomic Energy, P.O. Box 275, Beijing, P.R. China.
** Permanent address: Department of Nuclear Physics, Australian National University, G.P.O. Box 4, Canberra, ACT 2601, Australia.
*** Permanent address: Department of Physics, Panjab University, Chandigarh 160014, India.
**** Permanent address: Lawrence Livermore National Laboratory, P.O. Box 808, Livermore, CA 94550 L-396, USA.

on the magnetic dipole and electric quadrupole moments and it is interesting to determine these quantities up to high spins and to study the influence of alignments of neutrons and protons.

Connected with the different proton configurations are various shape effects. The slope of the single-particle energies as a function of quadrupole deformation determines the driving force towards larger (for $\partial E_\nu/\partial\beta_2 < 0$) or smaller (for $\partial E_\nu/\partial\beta_2 > 0$) nuclear deformation. In particular, it was predicted theoretically [18]) and confirmed experimentally [19,20]) that the strongly prolate-driving $[541]\frac{1}{2}^-$ $h_{9/2}$ and $[660]\frac{1}{2}^+$ $i_{13/2}$ proton configurations polarize the core to such an extent that the larger deformation has marked consequences e.g. on the alignment behavior mentioned above. Another interesting question concerns the occurrence of γ-softness [21,22]). The γ-deformation influences the energy-splitting of the coupled bands with different signature and all properties that depend on the signature splitting.

In this paper we report on the investigation of the high-spin states of ^{163}Lu. This nucleus lies in a region where γ-softness is predicted from calculations as well as from experimental systematics. In a previous study [3]) a strongly coupled band based on the $[514]\frac{9}{2}^-$ configuration and a decoupled band, for which the $[541]\frac{1}{2}^-$ configuration mentioned above was proposed, were identified up to medium spins. We extend these sequences to much higher spins and add another coupled band for which we suggest the $[404]\frac{7}{2}^+$ configuration, as well as a fragment of a second decoupled band. We are also able to connect the band structures to the low-spin states that were reported [23]) in a study of the radioactive decay of ^{163}Hf$\rightarrow$ ^{163}Lu. Furthermore, we present evidence that the first decoupled band may have a much larger deformation than the coupled bands and suggest that it may be built on the $[660]\frac{1}{2}^+$ proton $i_{13/2}$ configuration instead of the $[541]\frac{1}{2}^-$ $h_{9/2}$ structure suggested previously [3]).

The experimental procedure and data analysis are described in the following section. In sect. 3 the level scheme is presented, followed by a discussion of the nuclear structure properties of ^{163}Lu in sect. 4.

2. Experimental procedure and data analysis

High-spin states in ^{163}Lu were populated in the reaction ^{139}La(^{28}Si, 4n) at a bombarding energy of 150 MeV. The ^{28}Si beam was provided by the VICKSI accelerator of the HMI Berlin. At this energy the 4n and 5n exit channels are approximately equal in intensity. The targets consisted of foils of natural La, rolled to 1 mg/cm^2 thickness, that were protected by 30 μg/cm^2 Al evaporated on both sides. A target with backing was produced by evaporation of 8 mg/cm^2 Au onto a 1 mg/cm^2 La foil (and 30 μg/cm^2 Al on the front side).

Gamma-gamma coincidences were measured with the OSIRIS γ-ray spectrometer array which comprises 12 Compton-suppressed Ge detectors and an inner ball of 48 BGO detectors to measure γ-ray multiplicity and total energy. Gamma-ray

energies measured in the Ge detectors, the time of each Ge-signal with respect to the beam pulses from the accelerator, the number of BGO elements that showed a signal and their summed energy were recorded for each valid coincidence event. The majority of the events were two-fold coincidences between the Ge detectors (two γ-ray energies, two time signals as well as multiplicity and sum-energy signals from the BGO counters); about 7% were three-fold coincidences.

In the off-line analysis the event-by-event data from the 12 Ge detectors were carefully gain matched before they were sorted into two-dimensional E_γ-E_γ matrices (with the three-fold events unpacked). Only events that were prompt with respect to the beam pulse and for which more than 4 BGO detectors had fired were accepted in the sorting. With these conditions the matrices for the thin target and backed target experiments contained 68×10^6 and 28×10^6 events, respectively. In order to search for long-lived transitions (up to 100 ns) an E_γ-time matrix was sorted and to look for coincidences between these transitions an E_γ-E_γ matrix without any time condition was produced. A three-dimensional matrix of γ-ray energy, BGO sum energy and multiplicity, E_γ-H-K matrix, was useful to find assignments of γ-transitions to different reaction products. The three-fold coincidences were reordered according to increasing values of $E_{\gamma 1}$ for a faster access to produce double-gated spectra.

The γ-ray coincidence relationships were established by setting gates on the photopeaks of individual transitions and projecting the coincident spectra. Gates were also set on the background in the vicinity of the photopeaks in order to remove the background below the peaks of the gating transitions. Examples of the coincidence spectra are shown in figs. 1-3. The triple coincidences proved to be useful in resolving multiple transitions and placing them into the level scheme. Fig. 4 gives an example of triple coincidence spectra with no, one and two gates on the 197 keV multiplet.

The γ-ray intensities for transitions assigned to ^{163}Lu were determined from the total coincidence projections and from individual spectra in coincidence with low-spin transitions. For many levels spin assignments could be made on the basis of directional correlation ratios (DCO-ratios $I_\gamma(30°)/I_\gamma(90°)$) determined from the coincidence spectra. The coincidences between the four detectors at 30° and the two at 90° were sorted into a matrix with the 30° detectors on one and the 90° detectors on the other axis. By setting gates on several clean stretched E2 transitions on the 90° axis, coincidence spectra along the 30° axis were projected to determine $I_\gamma(30°)$. Similarly, in the transposed matrix, with gates on E2 transitions on the 30° axis, coincidence spectra along the 90° axis were projected to determine $I_\gamma(90°)$. The DCO-ratios $I_\gamma(30°)/I_\gamma(90°)$ are close to 1.0 for stretched E2 transitions and close to 0.7 for pure stretched dipole transitions. The level energies, γ-ray energies, intensities and spin assignments are summarized in table 1 and the DCO ratios for the strongly populated coupled band (labeled $[514]\frac{9^-}{2}$, see below) are given in table 2. DCO ratios could also be determined for several transitions in the other

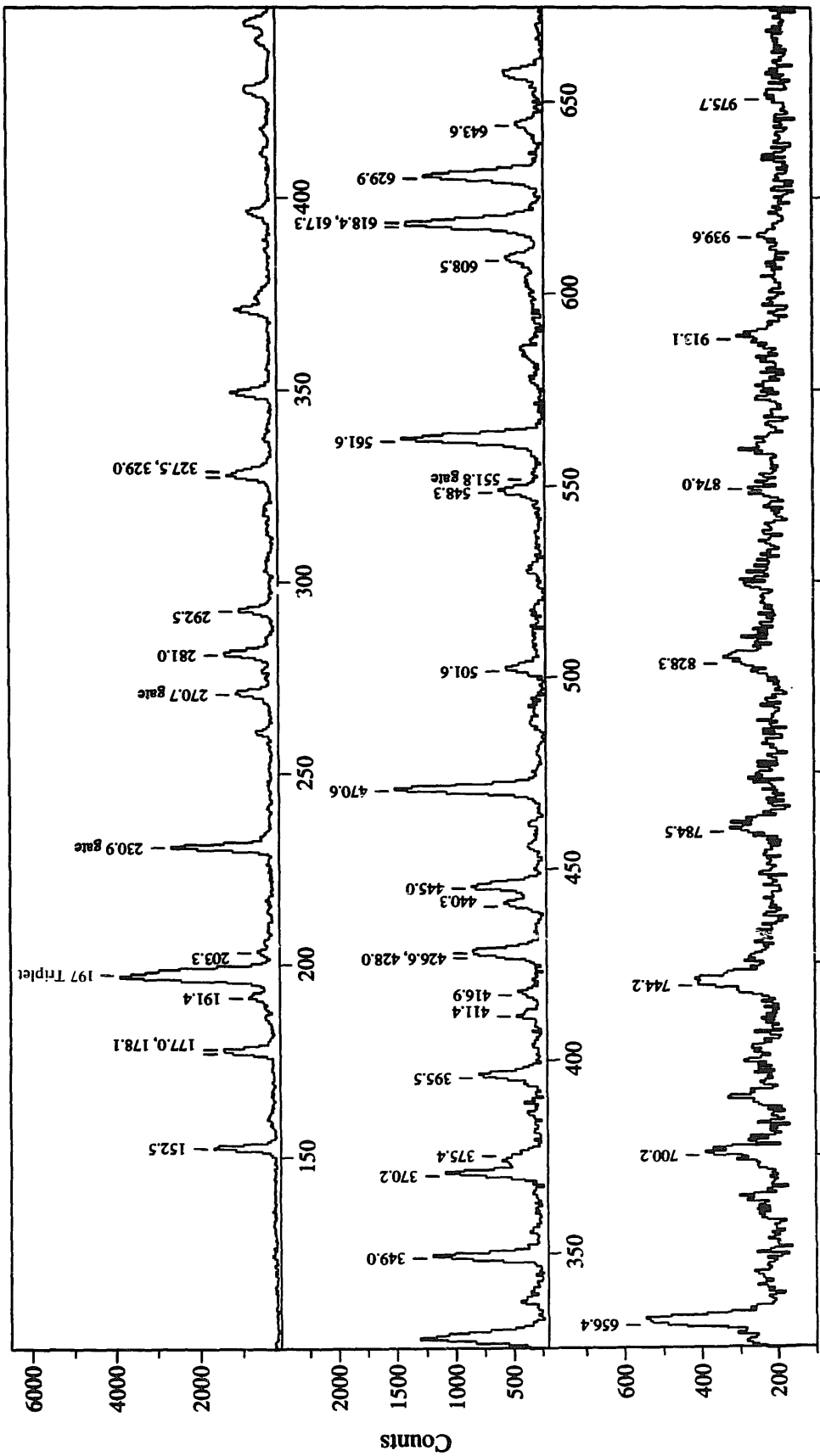

Fig. 1. Gamma-ray coincidence spectrum obtained with gates on the 231, 271 and 552 keV transitions of the $[514]\frac{9}{2}$ band of ^{163}Lu.

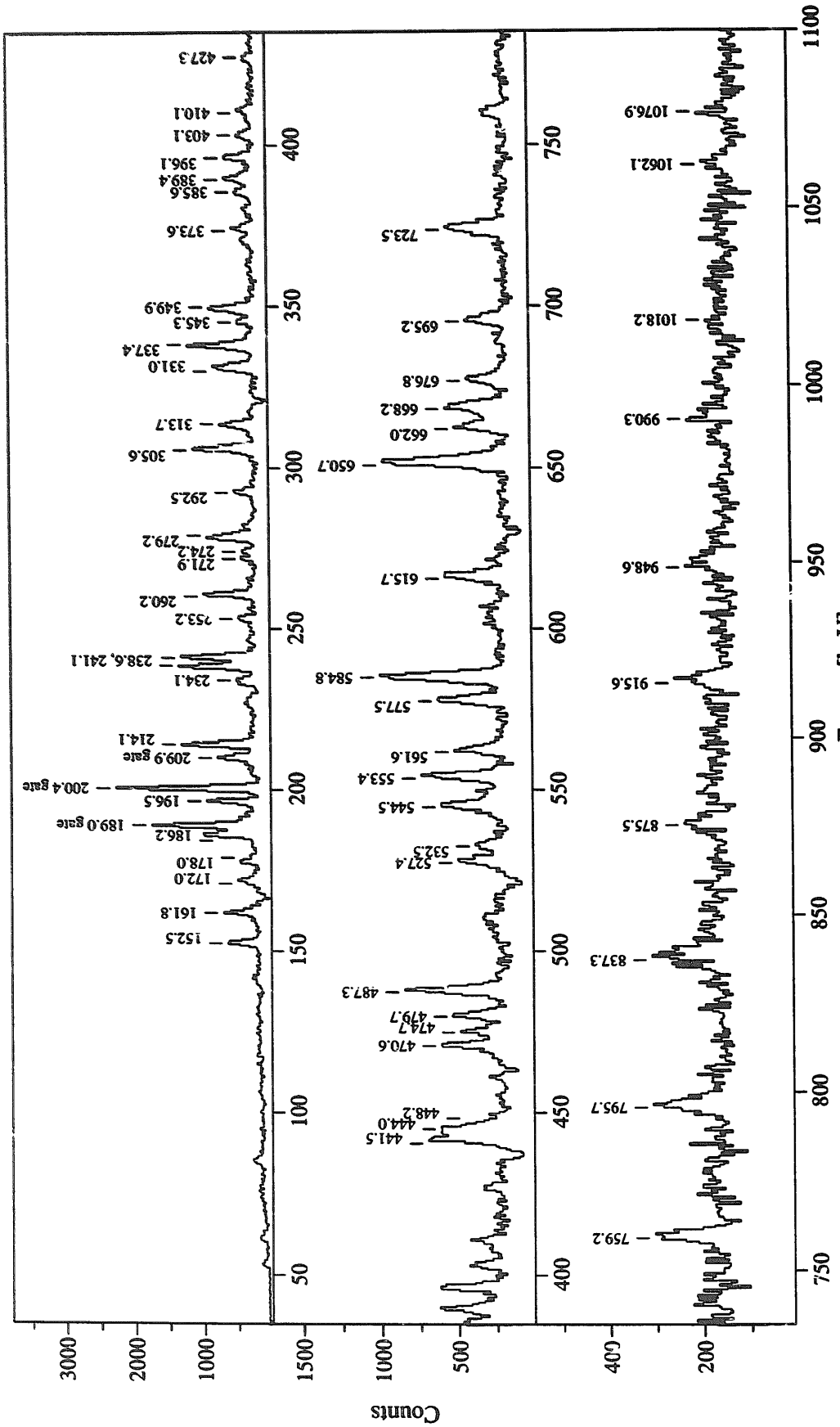

Fig. 2. Gamma-ray coincidence spectrum obtained with gates on the 189, 200 and 210 keV transitions of the $[404]\frac{7}{2}$ band of ^{163}Lu.

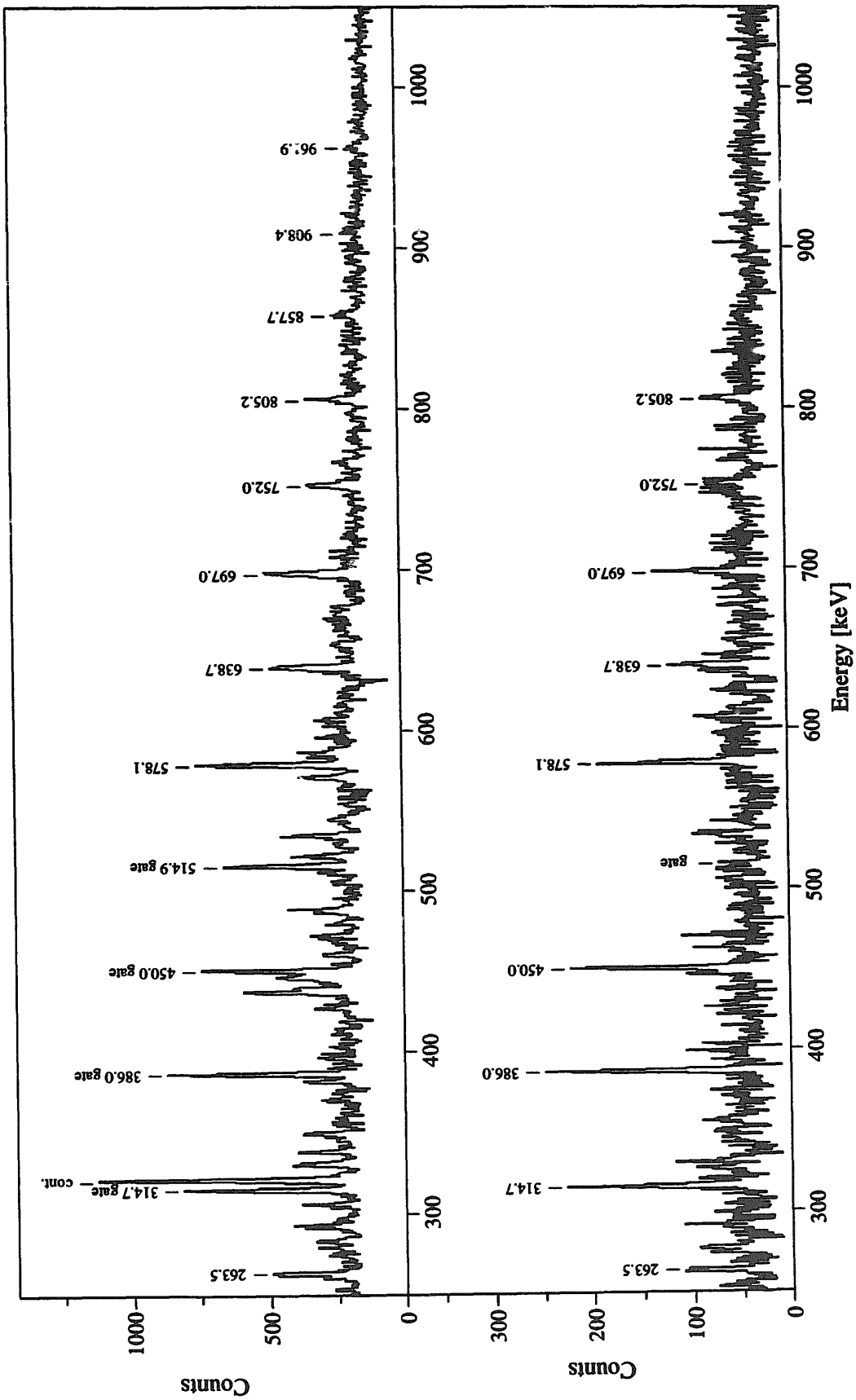

Fig. 3. Gamma-ray coincidence spectrum obtained with gates on the 315, 386, 450 and 515 keV transitions of the decoupled band (upper part) and with a single gate on the 515 keV transition in ^{163}Lu.

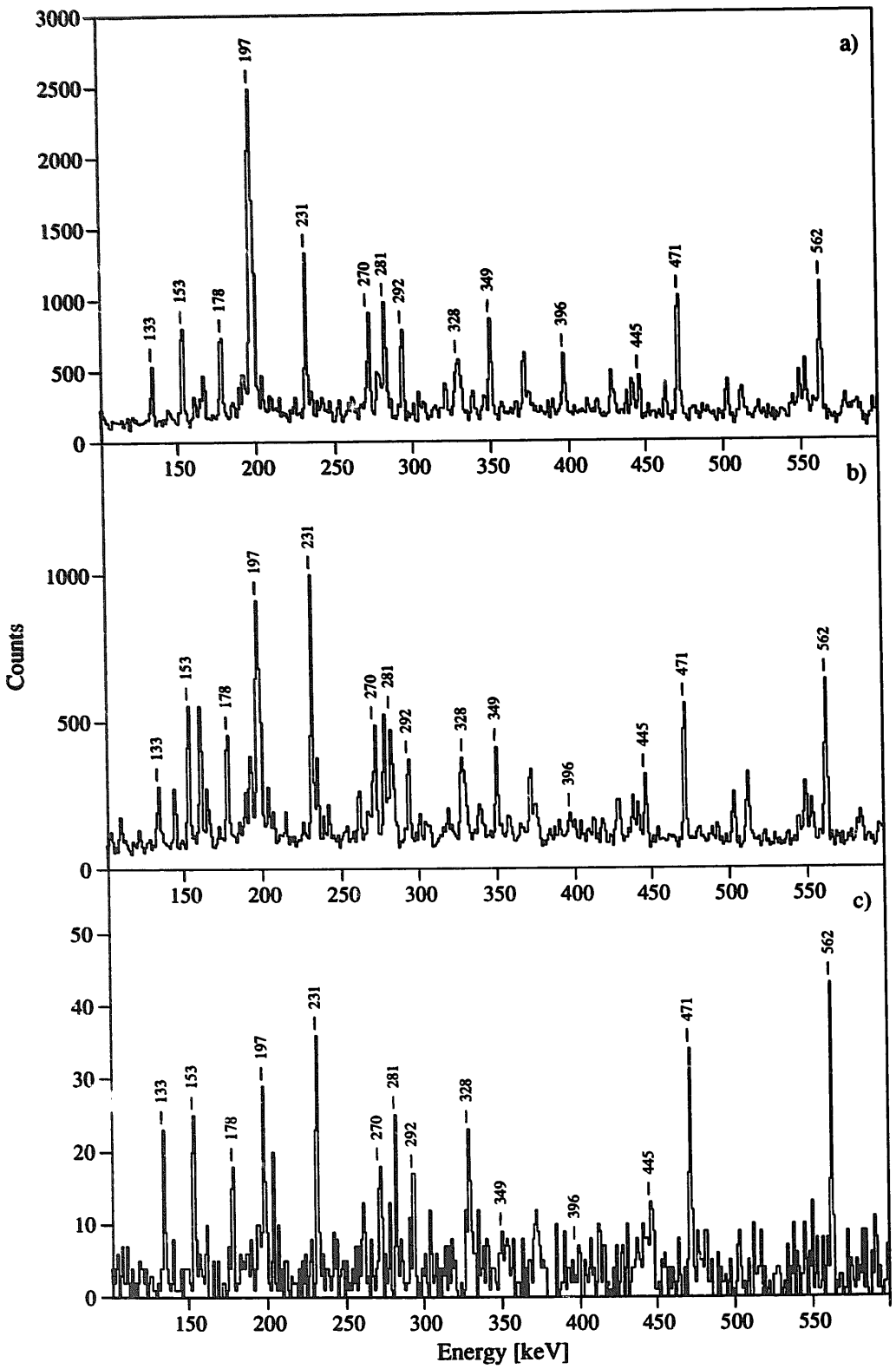

Fig. 4. Gamma-ray triple coincidence spectra, (a) total projection of all triple coincidences, (b) projection of triple coincidences with a single gate condition on the 197 keV line, (c) projection of triple coincidences with two gates on the 197 keV line.

TABLE 1

Level energies, spin assignments, γ-ray transition energies, intensities, branching ratios and $B(M1)/B(E2)$ ratios in ^{163}Lu

Level energy [keV]	Initial → final spin	Transition energy [keV] [a]	γ-ray intensity [b]	Branching ratio	$B(M1)/B(E2)$ [c]
(a) $[514]\frac{9}{2}^-$ band and connecting transitions to the ground state					
45.0		45.0 [d]			
107.0		62.0 [d]			
178.0		133.0 [d]			
		71.0 [d]			
263.8		85.8 [d]			
348.3	$\frac{11}{2}^- \rightarrow \frac{9}{2}^-$	84.5	170 (80)		
544.8	$\frac{13}{2}^- \rightarrow \frac{9}{2}^-$	281.0	105 (15)	0.290	0.554
	$\frac{13}{2}^- \rightarrow \frac{11}{2}^-$	196.5	362 (20)	(044)	(085)
697.3	$\frac{15}{2}^- \rightarrow \frac{11}{2}^-$	349.0	600 (20)	1.575	0.646
	$\frac{15}{2}^- \rightarrow \frac{13}{2}^-$	152.5	381 (30)	(135)	(054)
989.8	$\frac{17}{2}^- \rightarrow \frac{13}{2}^-$	445.0	390 (16)	0.907	0.536
	$\frac{17}{2}^- \rightarrow \frac{15}{2}^-$	292.5	430 (15)	(049)	(036)
1167.9	$\frac{19}{2}^- \rightarrow \frac{15}{2}^-$	470.6	1000 (20)	4.348	0.655
	$\frac{19}{2}^- \rightarrow \frac{17}{2}^-$	178.1	230 (38)	(724)	(109)
1538.1	$\frac{21}{2}^- \rightarrow \frac{17}{2}^-$	548.3	261 (32)	1.079	0.631
	$\frac{21}{2}^- \rightarrow \frac{19}{2}^-$	370.2	242 (25)	(173)	(102)
1729.5	$\frac{23}{2}^- \rightarrow \frac{19}{2}^-$	561.6	1059 (22)	7.564	0.734
	$\frac{23}{2}^- \rightarrow \frac{21}{2}^-$	191.4	140 (15)	(823)	(079)
2156.1	$\frac{25}{2}^- \rightarrow \frac{21}{2}^-$	618.0	240 (40)	1.270	0.637
	$\frac{25}{2}^- \rightarrow \frac{23}{2}^-$	426.6	189 (32)	(302)	(152)
2359.4	$\frac{27}{2}^- \rightarrow \frac{23}{2}^-$	629.9	863 (22)	10.79	0.763
	$\frac{27}{2}^- \rightarrow \frac{25}{2}^-$	203.3	80 (10)	(1.28)	(097)
2799.7	$\frac{29}{2}^- \rightarrow \frac{25}{2}^-$	643.6	239 (12)	1.707	0.528
	$\frac{29}{2}^- \rightarrow \frac{27}{2}^-$	440.3	140 (38)	(471)	(146)
2976.7	$\frac{31}{2}^- \rightarrow \frac{27}{2}^-$	617.3	897 (144)	6.79	1.696
	$\frac{31}{2}^- \rightarrow \frac{29}{2}^-$	177.0	135 (20)	(1.51)	(366)
3175.1	$\frac{33}{2}^- \rightarrow \frac{29}{2}^-$	375.4	81 (32)	0.195	3.409
	$\frac{33}{2}^- \rightarrow \frac{31}{2}^-$	198.4	415 (148)	(104)	(1.814)
	$\frac{33}{2}^- \rightarrow (\frac{29}{2}^-)$	268.1 [e]			
	$\frac{33}{2}^- \rightarrow (\frac{31}{2}^-)$	101.6 [e]			
2907.0	$(\frac{29}{2}^-) \rightarrow \frac{25}{2}^-$	750.9 [e]			
3372.2	$\frac{35}{2}^- \rightarrow \frac{31}{2}^-$	395.5	120 (40)	0.198	4.441
	$\frac{35}{2}^- \rightarrow \frac{33}{2}^-$	197.1	605 (221)	(098)	(2.197)
	$\frac{35}{2}^- \rightarrow (\frac{31}{2}^-)$	298.7 [e]			
3073.5	$(\frac{31}{2}^-) \rightarrow \frac{27}{2}^-$	714.1 [e]			
3603.1	$\frac{37}{2}^- \rightarrow \frac{33}{2}^-$	428.0	180 (22)	0.372	2.187
	$\frac{37}{2}^- \rightarrow \frac{35}{2}^-$	230.9	484 (20)	(047)	(282)
3873.8	$\frac{39}{2}^- \rightarrow \frac{35}{2}^-$	501.6	242 (20)	0.701	1.591
	$\frac{39}{2}^- \rightarrow \frac{37}{2}^-$	270.7	345 (15)	(066)	(149)
4154.9	$\frac{41}{2}^- \rightarrow \frac{37}{2}^-$	551.8	300 (25)	0.923	1.739
	$\frac{41}{2}^- \rightarrow \frac{39}{2}^-$	281.1	325 (40)	(137)	(258)
4482.3	$\frac{43}{2}^- \rightarrow \frac{39}{2}^-$	608.5	170 (35)	1.371	1.209
	$\frac{43}{2}^- \rightarrow \frac{41}{2}^-$	327.4	124 (36)	(488)	(429)
4811.3	$\frac{45}{2}^- \rightarrow \frac{41}{2}^-$	656.4	176 (15)	1.530	1.558
	$\frac{45}{2}^- \rightarrow \frac{43}{2}^-$	329.0	115 (12)	(206)	(210)
5182.5	$\frac{47}{2}^- \rightarrow \frac{43}{2}^-$	700.2	152 (20)	1.395	1.645
	$\frac{47}{2}^- \rightarrow \frac{45}{2}^-$	371.2	109 (25)	(369)	(434)

TABLE 1—continued

Level energy [keV]	Initial → final spin	Transition energy [keV] [a]	γ-ray intensity [b]	Branching ratio	$B(M1)/B(E2)$ [c]
5555.5	$\frac{49}{2}^- \rightarrow \frac{45}{2}^-$	744.2	220 (30)	2.444	1.254
	$\frac{49}{2}^- \rightarrow \frac{47}{2}^-$	375.3	90 (20)	(637)	(327)
5966.9	$\frac{51}{2}^- \rightarrow \frac{47}{2}^-$	784.5	143 (15)	1.375	2.163
	$\frac{51}{2}^- \rightarrow \frac{49}{2}^-$	411.4	104 (12)	(214)	(337)
6383.8	$\frac{53}{2}^- \rightarrow \frac{49}{2}^-$	828.3	160 (18)	1.684	2.227
	$\frac{53}{2}^- \rightarrow \frac{51}{2}^-$	416.9	95 (12)	(285)	(377)
6839.1	$\frac{55}{2}^- \rightarrow \frac{51}{2}^-$	872.2	119 (10)		
7296.9	$\frac{57}{2}^- \rightarrow \frac{53}{2}^-$	913.1	98 (10)		
7778.7	$\frac{59}{2}^- \rightarrow \frac{55}{2}^-$	939.6	100 (17)		
8260.5	$\frac{61}{2}^- \rightarrow \frac{57}{2}^-$	975.7	70 (8)		
(b) $[404]\frac{7}{2}^+$ *band*					
363.9	$\frac{9}{2}^+ \rightarrow \frac{7}{2}^+$	186.2	420 (25)		
573.8	$\frac{11}{2}^+ \rightarrow \frac{7}{2}^+$	396.1	221 (20)	1.661	0.442
	$\frac{11}{2}^+ \rightarrow \frac{9}{2}^+$	209.9	133 (10)	(196)	(052)
807.9	$\frac{13}{2}^+ \rightarrow \frac{9}{2}^+$	444.0	237 (20)	3.703	0.253
	$\frac{13}{2}^+ \rightarrow \frac{11}{2}^+$	234.1	64 (12)	(761)	(052)
1061.1	$\frac{15}{2}^+ \rightarrow \frac{11}{2}^+$	487.3	230 (30)	2.875	0.410
	$\frac{15}{2}^+ \rightarrow \frac{13}{2}^+$	253.2	80 (13)	(519)	(074)
1335.3	$\frac{17}{2}^+ \rightarrow \frac{13}{2}^+$	527.4	188 (19)	4.087	0.338
	$\frac{17}{2}^+ \rightarrow \frac{15}{2}^+$	274.2	46 (9)	(900)	(074)
1614.5	$\frac{19}{2}^+ \rightarrow \frac{15}{2}^+$	553.4	232 (15)	7.733	0.179
	$\frac{19}{2}^+ \rightarrow \frac{17}{2}^+$	279.2	30 (6)	(1.625)	(038)
1920.1	$\frac{21}{2}^+ \rightarrow \frac{17}{2}^+$	584.8	250 (30)	3.247	0.373
	$\frac{21}{2}^+ \rightarrow \frac{19}{2}^+$	305.6	77 (15)	(743)	(085)
2192.0	$\frac{23}{2}^+ \rightarrow \frac{19}{2}^+$	577.5	201 (18)	5.432	0.410
	$\frac{23}{2}^+ \rightarrow \frac{21}{2}^+$	271.9	37 (5)	(881)	(066)
2452.6	$\frac{25}{2}^+ \rightarrow \frac{21}{2}^+$	532.5	65 (6)	0.422	3.995
	$\frac{25}{2}^+ \rightarrow \frac{23}{2}^+$	260.6	154 (14)	(055)	(518)
	$\frac{25}{2}^+ \rightarrow \frac{23}{2}^-$	723.1	90 (10)		
2666.7	$\frac{27}{2}^+ \rightarrow \frac{23}{2}^+$	474.7	103 (8)	0.599	2.859
	$\frac{27}{2}^+ \rightarrow \frac{25}{2}^+$	214.1	172 (9)	(056)	(268)
2855.7	$\frac{29}{2}^+ \rightarrow \frac{25}{2}^+$	403.1	140 (12)	0.805	1.366
	$\frac{29}{2}^+ \rightarrow \frac{27}{2}^+$	189.0	174 (11)	(086)	(146)
3056.1	$\frac{31}{2}^+ \rightarrow \frac{27}{2}^+$	389.4	86 (5)	0.551	1.407
	$\frac{31}{2}^+ \rightarrow \frac{29}{2}^+$	200.4	156 (8)	(043)	(109)
3297.2	$\frac{33}{2}^+ \rightarrow \frac{29}{2}^+$	441.5	130 (20)	1.150	0.725
	$\frac{33}{2}^+ \rightarrow \frac{31}{2}^+$	241.1	113 (10)	(204)	(129)
3535.8	$\frac{35}{2}^+ \rightarrow \frac{31}{2}^+$	479.7	123 (6)	1.139	1.144
	$\frac{35}{2}^+ \rightarrow \frac{33}{2}^+$	238.6	108 (7)	(092)	(093)
3841.7	$\frac{37}{2}^+ \rightarrow \frac{33}{2}^+$	544.5	114 (10)	1.425	0.819
	$\frac{37}{2}^+ \rightarrow \frac{35}{2}^+$	305.9	80 (20)	(378)	(217)
4120.0	$\frac{39}{2}^+ \rightarrow \frac{35}{2}^+$	584.2	<150		
	$\frac{39}{2}^+ \rightarrow \frac{37}{2}^+$	278.3	<120		
4457.4	$\frac{41}{2}^+ \rightarrow \frac{37}{2}^+$	615.7	110 (15)	1.571	1.022
	$\frac{41}{2}^+ \rightarrow \frac{39}{2}^+$	337.4	79 (10)	(310)	(202)
4470.6	$\frac{43}{2}^+ \rightarrow \frac{39}{2}^+$	650.6	148 (40)	2.145	1.227
	$\frac{43}{2}^+ \rightarrow \frac{41}{2}^+$	313.7	69 (8)	(631)	(361)
5108.3	$\frac{45}{2}^+ \rightarrow \frac{41}{2}^+$	650.9	148 (40)	2.114	1.000
	$\frac{45}{2}^+ \rightarrow \frac{43}{2}^+$	337.7	70 (10)	(646)	(306)

TABLE 1—continued

Level energy [keV]	Initial → final spin	Transition energy [keV] [a])	γ-ray intensity [b])	Branching ratio	$B(M1)/B(E2)$ [c])
5438.8	$\frac{47}{2}^+ \rightarrow \frac{43}{2}^+$	668.2	111 (12)	1.850	1.390
	$\frac{47}{2}^+ \rightarrow \frac{45}{2}^+$	330.5	60 (20)	(648)	(487)
5770.3	$\frac{49}{2}^+ \rightarrow \frac{45}{2}^+$	662.0	108 (11)	1.964	1.239
	$\frac{49}{2}^+ \rightarrow \frac{47}{2}^+$	331.5	55 (20)	(742)	(468)
6115.6	$\frac{51}{2}^+ \rightarrow \frac{47}{2}^+$	676.8	103 (6)	1.689	1.424
	$\frac{51}{2}^+ \rightarrow \frac{49}{2}^+$	345.3	61 (5)	(170)	(143)
6465.5	$\frac{53}{2}^+ \rightarrow \frac{49}{2}^+$	695.2	102 (9)	2.684	0.984
	$\frac{53}{2}^+ \rightarrow \frac{51}{2}^+$	349.9	38 (7)	(548)	(201)
6839.1	$\frac{55}{2}^+ \rightarrow \frac{51}{2}^+$	723.5	55 (20)	0.873	3.035
	$\frac{55}{2}^+ \rightarrow \frac{53}{2}^+$	373.6	63 (5)	(325)	(1.130)
7224.7	$\frac{57}{2}^+ \rightarrow \frac{53}{2}^+$	759.2	86 (6)	2.457	1.248
	$\frac{57}{2}^+ \rightarrow \frac{55}{2}^+$	385.6	35 (3)	(272)	(138)
7634.8	$\frac{59}{2}^+ \rightarrow \frac{55}{2}^+$	795.7	70 (6)	0.986	3.269
	$\frac{59}{2}^+ \rightarrow \frac{57}{2}^+$	410.1	71 (10)	(163)	(540)
8062.1	$\frac{61}{2}^+ \rightarrow \frac{57}{2}^+$	837.3	85 (8)	1.771	2.076
	$\frac{61}{2}^+ \rightarrow \frac{59}{2}^+$	427.3	48 (5)	(249)	(292)
8510.3	$\frac{63}{2}^+ \rightarrow \frac{59}{2}^+$	875.5	86 (10)	4.30	0.926
	$\frac{63}{2}^+ \rightarrow \frac{61}{2}^+$	448.2	20 (10)	(2.21)	(476)
8977.7	$\frac{65}{2}^+ \rightarrow \frac{61}{2}^+$	915.6	40 (5)		
9458.9	$\frac{67}{2}^+ \rightarrow \frac{63}{2}^+$	948.6	50 (5)		
9968.0	$\frac{69}{2}^+ \rightarrow \frac{65}{2}^+$	990.3	41 (4)		
10477.1	$\frac{71}{2}^+ \rightarrow \frac{67}{2}^+$	1018.2	27 (5)		
11 030.1	$\frac{73}{2}^+ \rightarrow \frac{69}{2}^+$	1062.1	33 (4)		
11 554.0	$\frac{75}{2}^+ \rightarrow \frac{71}{2}^+$	1076.9	41 (7)		
12 147.5	$\frac{77}{2}^+ \rightarrow \frac{73}{2}^+$	1117.4	15 (15)		
12 676.8	$\frac{79}{2}^+ \rightarrow \frac{75}{2}^+$	1120.8	15 (15)		
13.307.9	$\frac{81}{2}^+ \rightarrow \frac{77}{2}^+$	1160.4	20 (15)		
14 533.3	$\frac{85}{2}^+ \rightarrow \frac{81}{2}^+$	1225.4			
(c) $[660]\frac{1}{2}^+$ band and connecting transitions to the ground state					
45.0		45.0 [d])			
173.8		173.8	<10		
206.9		161.9 [d])	<20		
503.4		329.6	25 (15)		
		296.5	<20		
950.4		447.0	35 (10)		
1484.3		533.9	50 (15)		
	$(\frac{17}{2}^+ \rightarrow \frac{13}{2}^+)$	264.6	30 (10)		
1799.0	$(\frac{21}{2}^+ \rightarrow \frac{17}{2}^+)$	314.7	81 (9)		
2185.0	$(\frac{25}{2}^+ \rightarrow \frac{21}{2}^+)$	386.0	95 (10)		
2635.0	$(\frac{29}{2}^+ \rightarrow \frac{25}{2}^+)$	450.0	95 (12)		
3149.9	$(\frac{33}{2}^+ \rightarrow \frac{29}{2}^+)$	514.9	100 (10)		
3728.0	$(\frac{37}{2}^+ \rightarrow \frac{33}{2}^+)$	578.1	105 (10)		
4366.7	$(\frac{41}{2}^+ \rightarrow \frac{37}{2}^+)$	638.7	95 (10)		
5063.7	$(\frac{45}{2}^+ \rightarrow \frac{41}{2}^+)$	697.0	90 (10)		
5815.7	$(\frac{49}{2}^+ \rightarrow \frac{45}{2}^+)$	752.0	70 (8)		
6620.9	$(\frac{53}{2}^+ \rightarrow \frac{49}{2}^+)$	805.2	52 (6)		
7478.6	$(\frac{57}{2}^+ \rightarrow \frac{53}{2}^+)$	857.7	33 (5)		
8387.0	$(\frac{61}{2}^+ \rightarrow \frac{57}{2}^+)$	908.4	14 (8)		
9348.9	$(\frac{65}{2}^+ \rightarrow \frac{61}{2}^+)$	961.9	26 (10)		

TABLE 1—continued

Level energy [keV]	Initial→ final spin	Transition energy [keV] [a])	γ-ray intensity [b])	Branching ratio	$B(M1)/B(E2)$ [c])
(*d*) *Decoupled band fragment* [f])					
206.9		161.9 [d])	<15		
232.6		232.6 [d])	50 (30)		
603.1		396.2	<20		
		370.5	50 (30)		
1088.8		485.7	60 (25)		
1651.6		562.8	40 (20)		
2258.5		606.9	35 (23)		

[a]) Uncertainties 0.3 keV, for weak transitions and multiple lines up to 1.0 keV.
[b]) Normalized to the 471 keV $\frac{19}{2}^- \rightarrow \frac{15}{2}^-$ transition, uncertainties 5-10%, for weak transitions and multiple lines up to 50%.
[c]) Determined assuming $\delta^2 = 0$.
[d]) Known from radioactive decay work [23]).
[e]) Intensities were below 4% relative to the 471 keV $\frac{19}{2}^- \rightarrow \frac{15}{2}^-$ transition.
[f]) Transitions stronger populated in the reaction $^{147}Sm(^{19}F, 3n)^{163}Lu$ with 85 MeV beam energy [24]).

bands. They confirm the assigned dipole or quadrupole character of the transitions, but the experimental uncertainties are rather large due to the complicated spectra with many unresolved doublets and/or low intensities of the transitions. We do not want to present these results in this work.

3. Level scheme

The level scheme of ^{163}Lu is presented in fig. 5. The decoupled band was reported by Honkanen *et al.* [3]) up to the spin-$\frac{45}{2}$ state at 5064 keV. We have extended this band to higher spins and found its connection to the 45 and 207 keV states that were established [23]) in the radioactive decay of ^{163}Hf. One strongly coupled band was also reported earlier [3]) and assigned as $[514]\frac{9}{2}^-$, but we have revised the level sequence in the band crossing region and extended it to higher spins. In our data we have no evidence for a 408 keV line reported by Honkanen *et al.* [3]). Instead, we have established the levels between 2977 and 3603 keV as shown in fig. 5. In the spectrum in coincidence with the 630 keV transition, which is parallel to the 427 keV transition, a narrow line of 428 keV can be seen. The same line shows up in the spectrum in coincidence with the 427 keV transition. In all other coincidence spectra with transitions of this band a broad 427/428 keV line is observed. It is clearly a doublet and we place the second transition (428 keV) above the level of 3175 keV. This band is connected to the states observed in the radioactive decay work [23]) by an 85/86 keV doublet. The low energy-part of the level-scheme is shown as "decay-part" in the insert at the upper left of fig. 5.

TABLE 2

DCO ratios for transitions in the $[514]^{9-}_{\frac{9}{2}}$ band

Level energy [keV]	Initial → final spin	Transition energy [keV]	$I_{\text{gate}=90°}(30°)/I_{\text{gate}=30°}(90°)$
E2 transitions			
544.8	$\frac{13}{2}^- \rightarrow \frac{9}{2}^-$	281.0	0.92 (13)
697.3	$\frac{15}{2}^- \rightarrow \frac{11}{2}^-$	349.0	0.82 (17)
1167.9	$\frac{19}{2}^- \rightarrow \frac{15}{2}^-$	470.6	1.16 (12)
1729.5	$\frac{23}{2}^- \rightarrow \frac{19}{2}^-$	561.6	1.01 (11)
2156.1	$\frac{25}{2}^- \rightarrow \frac{21}{2}^-$	618.0	0.95 (10)
2359.4	$\frac{27}{2}^- \rightarrow \frac{23}{2}^-$	629.9	1.21 (10)
2799.7	$\frac{29}{2}^- \rightarrow \frac{25}{2}^-$	643.6	1.00 (28)
2976.7	$\frac{31}{2}^- \rightarrow \frac{27}{2}^-$	617.3	0.95 (10)
3873.8	$\frac{39}{2}^- \rightarrow \frac{35}{2}^-$	501.6	0.94 (11)
4154.9	$\frac{41}{2}^- \rightarrow \frac{37}{2}^-$	551.8	0.82 (21)
4482.3	$\frac{43}{2}^- \rightarrow \frac{39}{2}^-$	608.5	1.16 (14)
4811.3	$\frac{45}{2}^- \rightarrow \frac{41}{2}^-$	656.4	1.03 (32)
M1 transitions			
544.8	$\frac{13}{2}^- \rightarrow \frac{11}{2}^-$	196.5	0.76 (20)
697.3	$\frac{15}{2}^- \rightarrow \frac{13}{2}^-$	152.5	0.80 (18)
989.8	$\frac{17}{2}^- \rightarrow \frac{15}{2}^-$	292.5	0.99 (24)
1167.9	$\frac{19}{2}^- \rightarrow \frac{17}{2}^-$	178.1	0.74 (20)
1538.1	$\frac{21}{2}^- \rightarrow \frac{19}{2}^-$	370.2	0.82 (18)
1729.5	$\frac{23}{2}^- \rightarrow \frac{21}{2}^-$	191.4	0.86 (18)
2976.7	$\frac{31}{2}^- \rightarrow \frac{29}{2}^-$	177.0	0.74 (20)
3175.1	$\frac{33}{2}^- \rightarrow \frac{31}{2}^-$	198.4	0.76 (20)
3372.2	$\frac{35}{2}^- \rightarrow \frac{33}{2}^-$	197.1	0.76 (20)
3603.1	$\frac{37}{2}^- \rightarrow \frac{35}{2}^-$	230.9	0.71 (18)
3873.8	$\frac{39}{2}^- \rightarrow \frac{37}{2}^-$	270.7	0.80 (15)
4154.9	$\frac{41}{2}^- \rightarrow \frac{39}{2}^-$	281.1	0.92 (13)
4482.3	$\frac{43}{2}^- \rightarrow \frac{41}{2}^-$	327.4	0.80 (18)
4811.3	$\frac{45}{2}^- \rightarrow \frac{43}{2}^-$	329.0	0.80 (18)

The analysis of the triple coincidences establishes that three transitions of about 197 keV occur in the $[514]^{9-}_{\frac{9}{2}}$ band (see fig. 4). In the spectrum in coincidence with the 396 keV transition, which we place parallel to the 197 and 198 keV transitions, a narrow line of 196.5 keV can be seen, which is the $\frac{13}{2}^- \rightarrow \frac{11}{2}^-$ transition reported earlier [3]). In the spectrum in coincidence with the 428 keV transition the 196.5 and 198.4 keV lines are resolved and the 197.1 keV transition is missing because it is parallel to the gating transition. Another unresolved doublet is the line at about 328 keV. In the spectra in coincidence with the 700 keV transition a narrow line of 327 keV is observed and with the 609 keV transition a line of 329 keV is seen. In a similar way the two other doublets of about 281 and 618 keV could be placed into the level scheme.

The second strongly coupled band for which we make the assignment $[404]^{7+}_{\frac{7}{2}}$, see discussion below, was not known from the previous work [3]). A number of

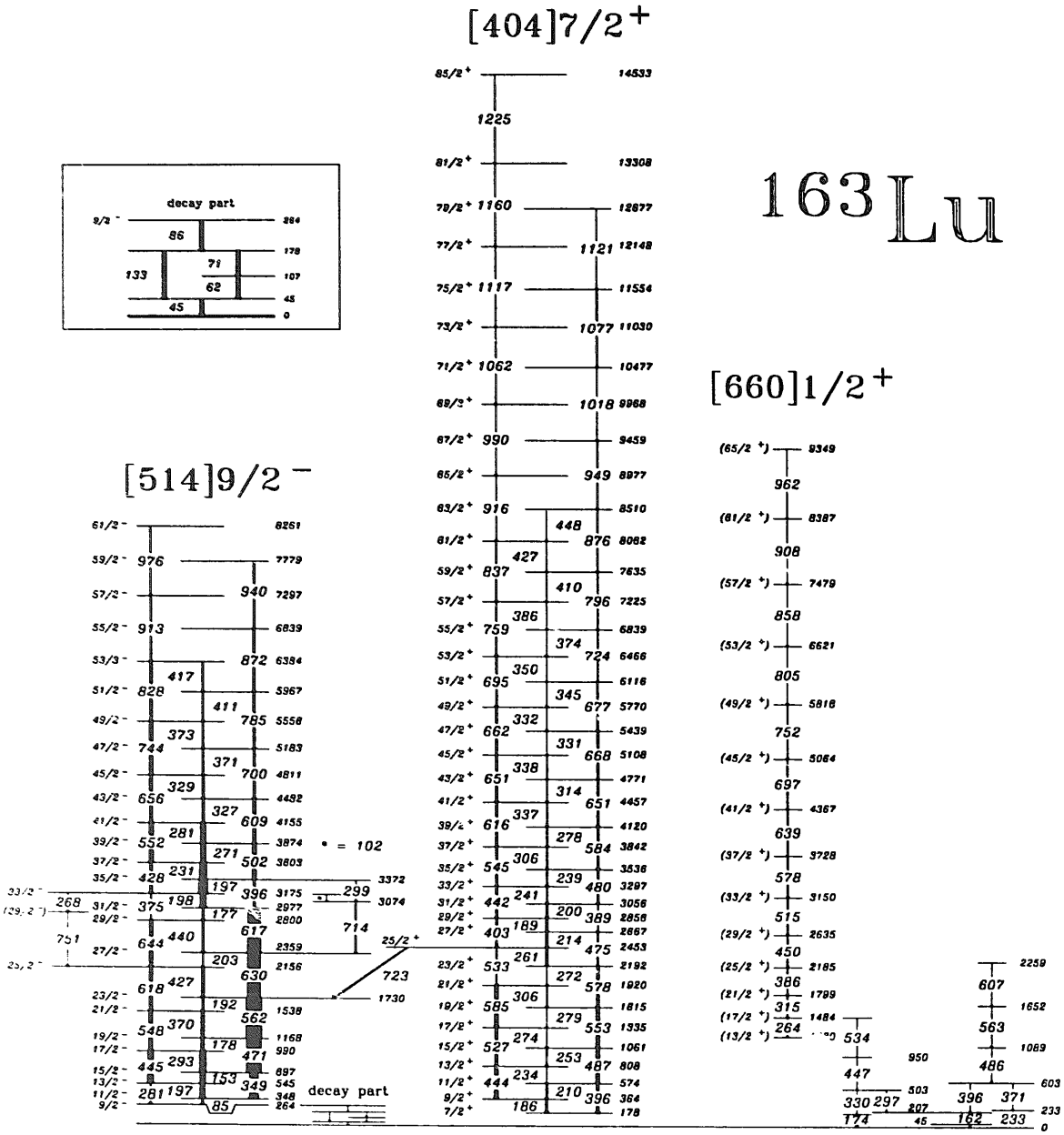

Fig. 5. Level scheme of ^{163}Lu. Insert at upper left: low energy part of the level scheme of ^{163}Lu from radioactive decay work [23]).

unresolved doublets with energies of 279, 306, 337, 584 and 651 keV appear in this sequence. Their placement into the level scheme could be determined uniquely on the basis of the double and triple coincidence data. This band is connected to the $[514]^{9-}_{2}$ band by the 723 keV $\frac{25+}{2} \rightarrow \frac{23-}{2}$ transition which has a DCO ratio of 0.58 (22) and is therefore assigned as a stretched dipole. Further connections are likely, but could not be established because of intensity limitations. The 723 keV transition fixes the energies of the $[404]^{7+}_{2}$ band relative to the remaining level scheme as well as spins and parities. The decay of the 178 keV level to the ground state could not be found.

In a later experiment [24]) we have established a fragment of a second decoupled band that was not observed previously with transition energies of 486, 563 and 607 keV. The transitions of 492 and 578 keV probably have to be placed on top of that sequence but their assignments are difficult because they are not clean lines and rather weak. At low spins this sequence is connected to the 162 keV transition known from the radioactive decay work [23]). In the reaction ^{139}La(^{19}F, 3n)^{163}Lu this band is populated only with an intensity of about 40% of that of the more strongly populated decoupled band.

The spin and parity assignments are partly based on the DCO ratios given in table 2, the observed connections to the previously known [23]) low-spin states and on the considerations presented below. Our assignments for the strongly populated coupled band that is yrast at lower spins are in agreement with the work of Honkanen *et al.* [3]) who suggests that it is based on the $h_{11/2}[514]^{9-}_{2}$ proton state. There are two negative-parity Nilsson orbits, the $[514]^{9-}_{2}$ and the $[523]^{7-}_{2}$ levels, close to the Fermi surface in ^{163}Lu and on the basis of our data we cannot really determine which is the correct assignment. For bands built on the $h_{11/2}$ proton states the favoured signature is $\alpha_f = -\frac{1}{2}$ and the favoured and unfavoured sequences have spins $I_f = \frac{3}{2}, \frac{7}{2}, \frac{11}{2}, \ldots$ and $I_u = \frac{1}{2}, \frac{5}{2}, \frac{9}{2}, \ldots$, respectively. The lowest observed state in this band, $I = \frac{9}{2}^-$, belongs to the unfavoured signature sequence. In the favoured sequence no level below the $\frac{11}{2}^-$ state was observed. Therefore, this band is most likely built on the $[514]^{9-}_{2}$ Nilsson state, as in the neighbouring ^{165,167}Lu isotopes [2,4]). Furthermore, this assignment is in agreement with the systematic trend of transition energies between corresponding states [1,2,4]) in $^{161-167}$Lu.

4. Discussion

4.1. TRANSITION PROBABILITIES

For the two strongly coupled bands the ratios of reduced transition probabilities for $\Delta I = 1$ and $\Delta I = 2$ γ-ray transitions

$$\frac{B(\mathrm{M1}, \Delta I = 1)}{B(\mathrm{E2}, \Delta I = 2)} = c\frac{E_\gamma(\Delta I = 2)^5}{E_\gamma(\Delta I = 1)^3}\frac{1}{\lambda(1+\delta^2)} \qquad \text{with } c = 0.697\ \mathrm{MeV}^{-2}\cdot\mu^2/e^2\mathrm{b}^2$$

are determined up to high spins from the intensity branching ratios λ. The γ-ray energies are given in MeV and δ is the E2/M1 mixing ratio of the $\Delta I = 1$ transitions. In principle the mixing ratios can be determined from the γ-ray directional correlations, e.g. DCO ratios. For the $[514]^{9-}_{2}$ band the DCO ratios given in table 2 lie between 0.7 an 0.8. For pure stretched dipole transitions we calculate 0.65 for our geometry. The larger experimental ratios indicate small positive E2/M1 mixing ratios ($\delta \simeq 0.15$) and we can neglect δ^2. For simplicity we have also set $\delta^2 = 0$ for the $[404]^{7+}_{2}$ band. The experimental $B(\mathrm{M1})/B(\mathrm{E2})$ ratios for the two strongly coupled

bands are included in table 1. They can be compared to the theoretical expression [25])

$$\frac{B(\mathrm{M1})}{B(\mathrm{E2})} = \frac{12}{5Q_0^2\cos^2(30°+\gamma)}\left(1-\frac{K^2}{(I-\frac{1}{2})^2}\right)^{-2} K^2 \times\left[(g_p-g_R)\left(\sqrt{1-\left(\frac{K}{I}\right)^2}-\frac{i_p}{I}\pm\frac{\Delta e}{\omega}\right)-(g_n-g_R)\frac{i_n}{I}\right]^2,$$

which is valid only for small γ-deformation. The curves shown in fig. 6 have been calculated using theoretical g-factors ($g_R = 0.4$, $g_n = -0.25$, $g_p = 1.30$ for $[514]^{9-}_{2}$, $g_p = 0.62$ for $[404]^{7+}_{2}$), the experimental signature splitting Δe and alignments i from our work and a constant quadrupole moment of $6e \cdot$ b. The γ-deformation has been set to 0° for the $[404]^{7+}_{2}$ band and for the $[514]^{9-}_{2}$ band above the band crossing. Below the band crossing the latter band shows a large signature splitting which is probably due to γ-deformation (see below) and therefore no comparison to the theoretical expression is shown in fig. 6. Reasonable agreement is obtained for the $[404]^{7+}_{2}$ band using the proton g-factors for this configuration, but the $[402]^{5+}_{2}$ configuration (with $g_p = 1.56$) for the positive-parity band is ruled out.

Hagemann *et al.* [22]) derived a relation between the signature splitting Δe and the difference of $B(\mathrm{M1})$ values $\Delta B(\mathrm{M1}) = B(\mathrm{M1}, \alpha_f \to \alpha_u) - B(\mathrm{M1}, \alpha_u \to \alpha_f)$ where α_f and α_u are the favoured and unfavoured signatures, respectively,

$$\frac{\Delta B(\mathrm{M1})}{B(\mathrm{M1})_{av}} = \frac{4\Delta e\hbar\omega}{(\Delta e)^2+(\hbar\omega)^2}.$$

This relation holds only for axially symmetric nuclei. Comparison with experimental data showed good agreement for a chain of Yb isotopes where no γ-deformation is expected. For the Lu isotopes agreement is obtained for the heavy ^{167}Lu, but large deviations are found for the lighter isotopes [22]). In the $[514]^{9-}_{2}$ band

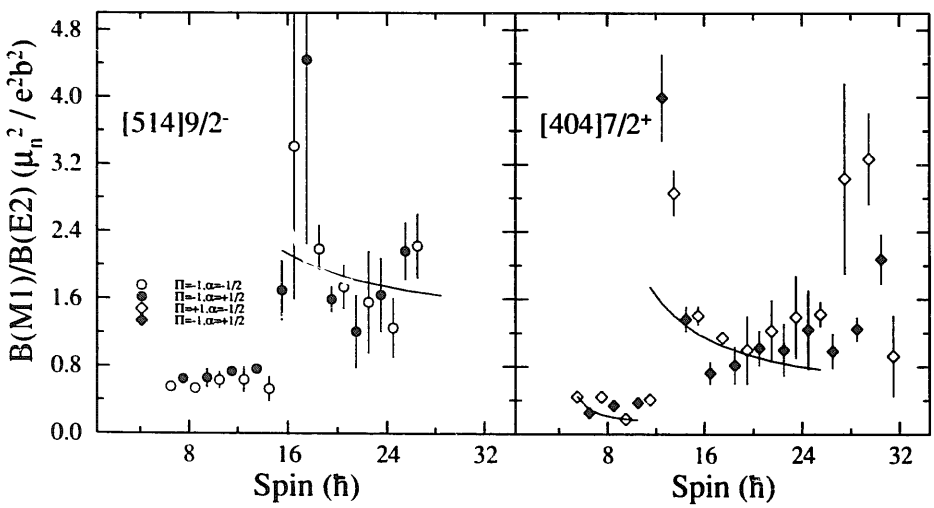

Fig. 5. Ratios of reduced transition probabilities $B(\mathrm{M1})/B(\mathrm{E2})$ for the strongly coupled bands in ^{163}Lu. The curves were obtained with calculated g-factors and with the experimental alignments and signature splittings determined in this work (see text).

in ^{163}Lu the deviation between B(M1) ratios and signature splitting is large below the band crossing and we take this as an indication for a sizeable γ-deformation. Therefore, the theoretical expression for the B(M1)/B(E2) ratios does not reproduce the experimental values in the low-spin region.

4.2. BAND CROSSINGS AND ALIGNMENTS

The cranked shell model [26]) (CSM) is very successful in describing high-spin features like band-crossing frequencies, rotation aligned angular momenta and signature splittings of many nuclei. In order to compare the properties of the observed rotational bands to the results of CSM calculations, the experimental quantities must be transformed into the rotating frame. As core of reference for that transformation the Harris expansion for the projection of the angular momentum on an axis perpendicular to the symmetry axis of the nucleus (x-axis) is used [26]):

$$I_x^{\mathrm{ref}} = i_0 + J_0\omega + J_1\omega^3 .$$

The experimental values of I_x are given by

$$I_x \approx \sqrt{(I+\tfrac{1}{2})^2 - K^2} .$$

The frequency of rotation around the x-axis of the nucleus

$$\hbar\omega(I) = \frac{\mathrm{d}E(I)}{\mathrm{d}I_x} ,$$

is obtained from the experimental spectra by

$$\hbar\omega(I) = \frac{E_\gamma}{I_x(I+1) - I_x(I-1)} \approx \tfrac{1}{2}E_\gamma .$$

The experimental routhians and aligned angular momenta for the $[514]^{9-}_{2}$ and $[404]^{7+}_{2}$ bands are plotted in figs. 7 and 8, respectively. The Harris parameters

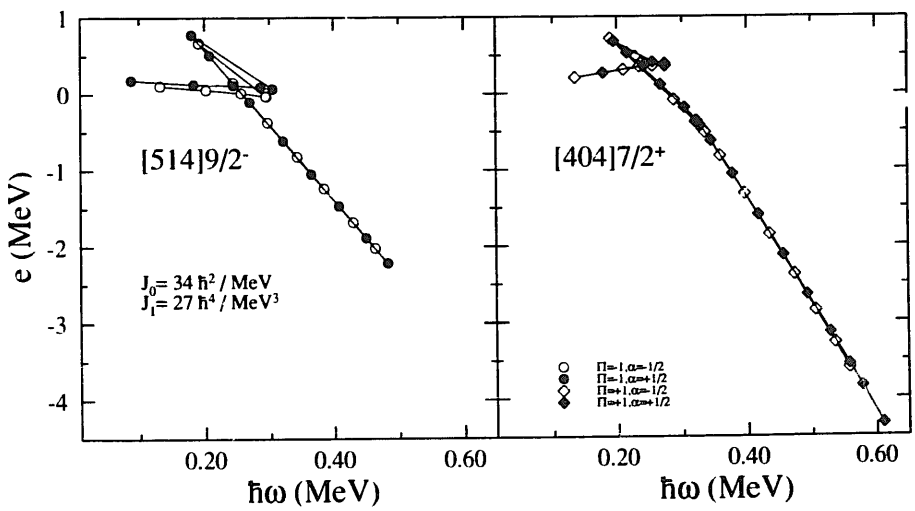

Fig. 7. Experimental routhians for the $[514]^{9-}_{2}$ and $[404]^{7+}_{2}$ bands in ^{163}Lu.

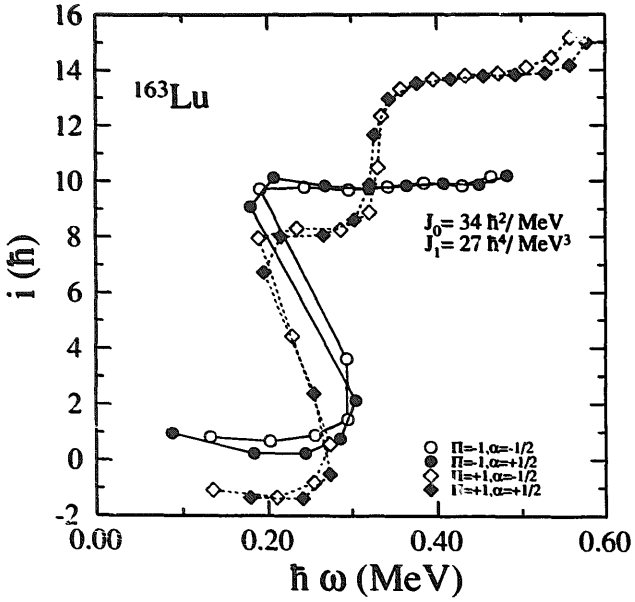

Fig. 8. Experimental aligned angular momenta for the $[514]^{9-}_{2}$ and $[404]^{7+}_{2}$ bands in ^{163}Lu.

$J_0 = 34\hbar^2/\mathrm{MeV}$ and $J_1 = 27\hbar^4/\mathrm{MeV}^3$ were obtained by fits of the expression for the reference core to the high-spin states of these bands.

The experimental routhians in fig. 7 show a signature splitting for the $[514]^{9-}_{2}$ band of $\Delta e = 120$ keV below the band crossing which reverses and is much smaller above the band crossing. The $[404]^{7+}_{2}$ band shows almost no signature splitting over the whole frequency range. The signature splitting can be made visible in the more sensitive plot of $E_\gamma(I \to I-1)/2I$ as a function of spin, as shown in fig. 9.

The experimental alignments shown in fig. 8 exhibit a strong backbending in both bands around $\hbar\omega = 0.25$ MeV which is caused by the alignment of a pair of $i_{13/2}$ neutrons (see comparison to the results of the CSM calculations below). At a

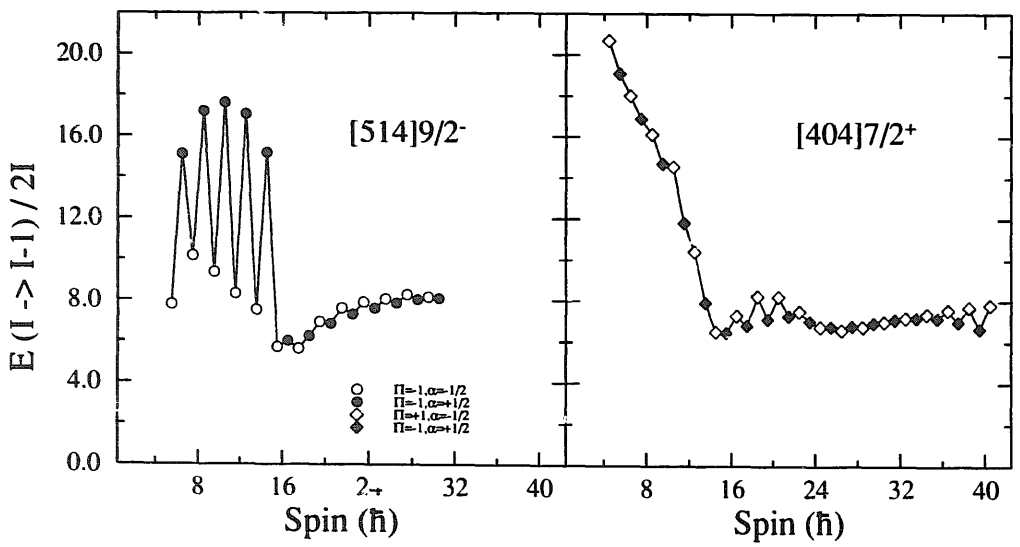

Fig. 9. $E_\gamma(I \to I-1)/2I$ as a function of spin for the coupled bands in ^{163}Lu.

surprisingly low frequency of $\hbar\omega = 0.33$ MeV a second bandcrossing is observed in the $[404]^{7+}_{\frac{7}{2}}$ band which is absent in the $[514]^{9-}_{\frac{9}{2}}$ band. This behaviour can be explained if we assume that the second band crossing is caused by $h_{11/2}$ protons that are blocked in the $[514]^{9-}_{\frac{9}{2}}$ band. A lowering of the proton crossing frequencies compared to the even Z-neighbours is expected in the odd-proton system due to the blocking effect resulting in a decreased pairing energy. In odd-neutron nuclei the lowering of the $i_{13/2}$ neutron crossing frequency was investigated for many cases [27]) and found to be around 14% compared to the even systems. In the odd-Z nuclei the reduction is expected to be even larger, around 20%, because of the lower density of proton levels in this mass region. Indeed, our CSM calculations presented in the following chapter give a rather low frequency for the $h_{11/2}$ proton alignment, but do not fully reproduce the experimental frequency using only these considerations.

4.3. CSM CALCULATIONS

For our CSM calculations a computer code supplied to us by Dudek and Nazarewicz [28,29]) was used. It employs a deformed Woods-Saxon potential with parameters which provide a good description of the single-particle levels and the shell structure for both spherical and deformed nuclei. Starting values for the deformation parameters were obtained for the different configurations from total routhian surface (TRS) calculations [30,31]). Selected examples of the results of the TRS calculations are presented in fig. 10. As can be seen, the calculated surface of the negative-parity $[514]^{9-}_{\frac{9}{2}}$ band is γ-soft below the neutron $i_{13/2}$ alignment (with a minimum at $\gamma = -3.4°$, upper left of fig. 10), but it becomes more γ-stable with $\gamma \simeq 0°$ above that crossing (center left of fig. 10). Note that the soft potential will lead to dynamical configuration mixing which is not accounted for in the static TRS calculations. The calculated surfaces for the positive-parity $[404]^{7+}_{\frac{7}{2}}$ band is γ-stable with γ-values close to zero at all frequencies (upper and center right of fig. 10). This difference in γ-deformation and γ-softness in the TRS calculations qualitatively describes the different behaviour of the $[514]^{9-}_{\frac{9}{2}}$ and the $[404]^{7+}_{\frac{7}{2}}$ bands, although the experimental signature splitting and $B(M1)/B(E2)$ ratios indicate larger negative γ-values for the $[514]^{9-}_{\frac{9}{2}}$ band (see above). One reason for the discrepancy is that the calculations do not follow the single-quasiparticle bands up to higher frequencies where the signature splitting gets larger.

In order to investigate the dependence of the band crossing frequency on the deformation, the parameters were varied over a wide range in the CSM calculations. As examples, the calculated $i_{13/2}$ neutron and $h_{11/2}$ proton band crossing frequencies are plotted as a function of the deformation parameter β_2 for different values of γ in fig. 11. In these calculations the neutron pairing was kept constant with $\Delta = 1.02$ MeV calculated from the odd-even mass differences. As can be seen, a slightly higher neutron $i_{13/2}$ crossing frequency is calculated for negative values of the γ-deformation (for small β_2) which can explain the higher band crossing frequency

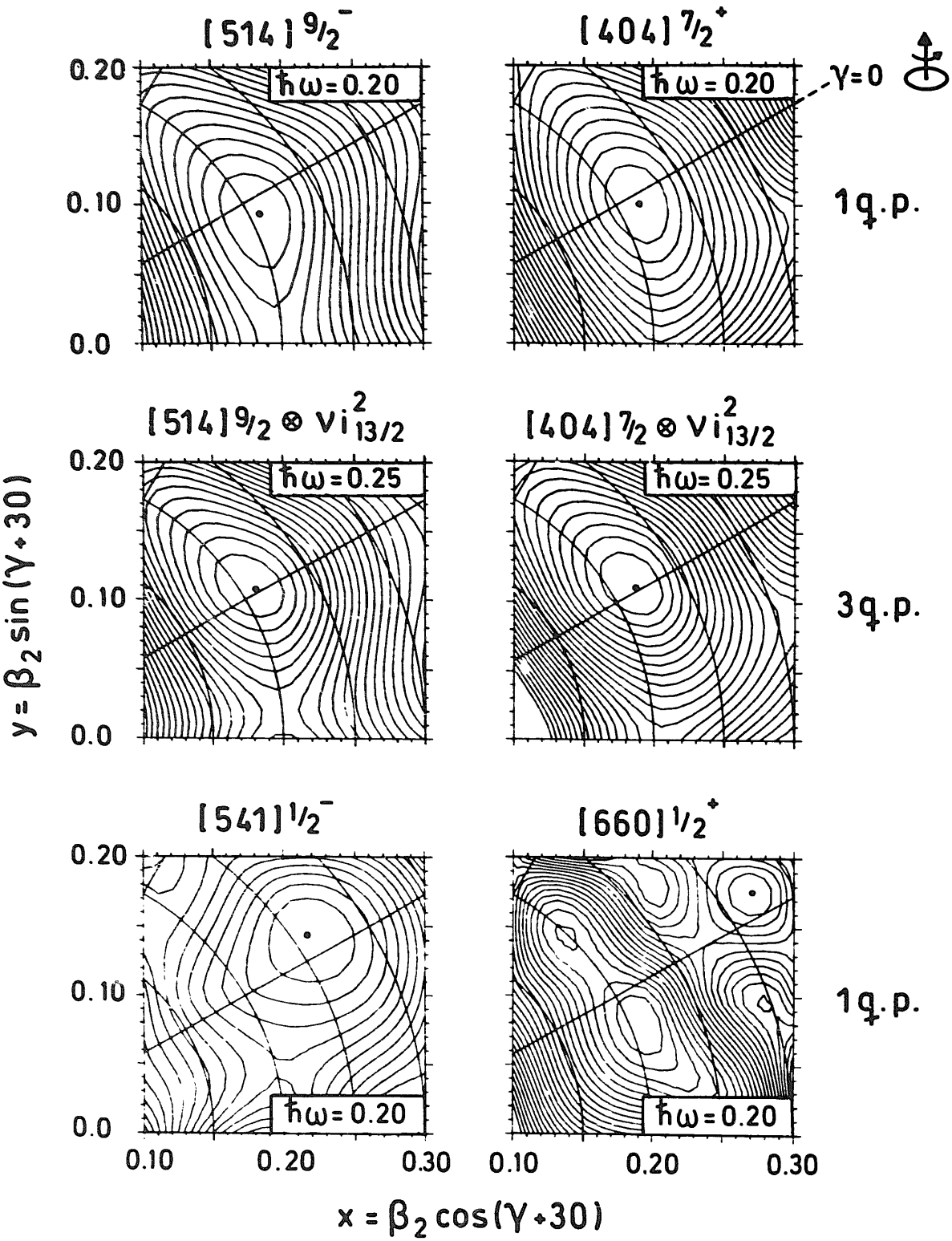

Fig. 10. Proton total routhian surfaces (TRS) calculated for the $[514]^{9^-}_{\frac{9}{2}}$ and $[404]^{7^+}_{\frac{7}{2}}$ configurations before (at $\hbar\omega = 0.20$ MeV) and after ($\hbar\omega = 0.25$ MeV) and neutron $i_{13/2}$ alignment and for the high-j intruder states $[541]^{1^-}_{\frac{1}{2}}$ and $[660]^{1^+}_{\frac{1}{2}}$.

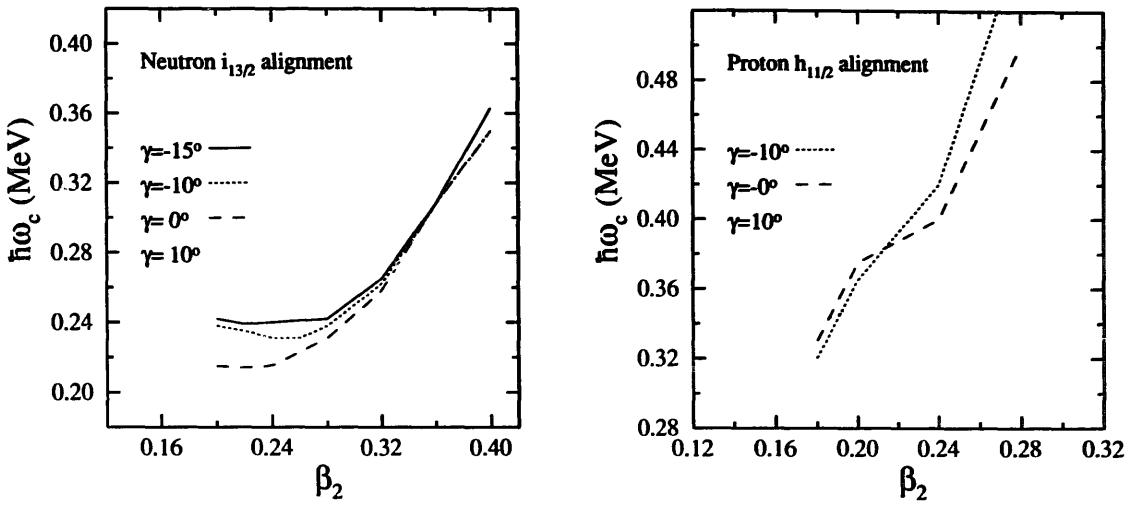

Fig. 11. Neutron $i_{13/2}$ and proton $h_{11/2}$ band crossing frequencies as a function of the deformation parameters β_2 for different values of γ-deformation.

observed for the $[514]^{9-}_{2}$ band (see fig. 8). For the proton pairing a reduced value of $\Delta_p = 0.80$ MeV was chosen because of blocking [27]) and level density arguments. The right panel of fig. 11 shows that the crossing frequency decreases steeply with decreasing quadrupole deformation. The alignment of a pair of $h_{11/2}$ protons in the upper part of that shell drives the nucleus towards smaller deformation and it seems therefore appropriate to use $\beta_2 = 0.2$. With these parameters we obtain $\hbar\omega = 0.37$ MeV for the proton crossing frequency which is still somewhat higher than the experimental value of 0.33 MeV. A comparison of experimental and theoretical crossing frequencies and alignments is made in table 3.

4.4. THE DECOUPLED BANDS

The strongly populated decoupled sequence in ^{162}Lu was previously interpreted [3]) as the $[541]^{1-}_{2}$ $h_{9/2}$ proton band that is systematically observed in this mass region [1]). We extend this band up to a rotational frequency of $\hbar\omega = 0.48$ MeV. The aligned angular momentum as a function of rotational frequency is plotted for this band in fig. 12. If we use the same reference core for this band as for the strongly coupled bands (see above) we obtain a linearly increasing alignment curve, see fig. 12 (full circles). It may be that this is evidence for a gradual alignment caused by a band crossing with a very large interaction energy [19]). However, we want to suggest an alternative explanation for the behaviour of the decoupled band. Fig. 13 shows the dynamic moments of inertia

$$J^{(2)} = \left(\frac{\partial^2 E}{\partial I^2}\right)^{-1} \simeq \frac{4\hbar^2}{\Delta E_\gamma}$$

for the decoupled band and for the two strongly coupled bands outside the band-crossing region. Clearly, the decoupled band has a much larger moment of inertia

TABLE 3

Calculated and experimental band crossing frequencies and alignments

	Calculated		Experimental	
	$\hbar\omega_c$ (MeV)	Δi ($\hbar$)	$\hbar\omega_c$ (MeV)	Δi ($\hbar$)
$\Delta_n = 1.02$ MeV, $\beta_2 = 0.22$				
$\gamma = 0°$	0.212	9.9		
$\gamma = -10°$	0.226	9.6		
$\gamma = -20°$	0.250	9.3		
$[514]^{9-}_{\frac{9}{2}}$, $\alpha_f = -\frac{1}{2}$,				
$i_{13/2}$ neutron crossing			0.255	9.2
$[514]^{9-}_{\frac{9}{2}}$, $\alpha_u = +\frac{1}{2}$,				
$i_{13/2}$ neutron crossing			0.264	9.6
$[404]^{7+}_{\frac{7}{2}}$, $\alpha_f = +\frac{1}{2}$,				
$i_{13/2}$ neutron crossing			0.235	9.5
$[404]^{7+}_{\frac{7}{2}}$, $\alpha_u = -\frac{1}{2}$,				
$i_{13/2}$ neutron crossing			0.235	9.5
$\Delta_n = 0.80$ MeV, $\beta_2 = 0.22$, $\gamma = 0°$	0.404	4.2		
$[404]^{7+}_{\frac{7}{2}}$, $\alpha_f = +\frac{1}{2}$,				
$h_{11/2}$ proton crossing			0.33	5.2
$[404]^{7+}_{\frac{7}{2}}$, $\alpha_u = -\frac{1}{2}$,				
$h_{11/2}$ proton crossing			0.33	5.2
$\Delta_n = 1.02$ MeV, $\beta_2 = 0.33$, $\gamma = 0°$	0.270	8.4		
$[660]^{1+}_{\frac{1}{2}}$, $i_{13/2}$ neutron crossing			>0.48	

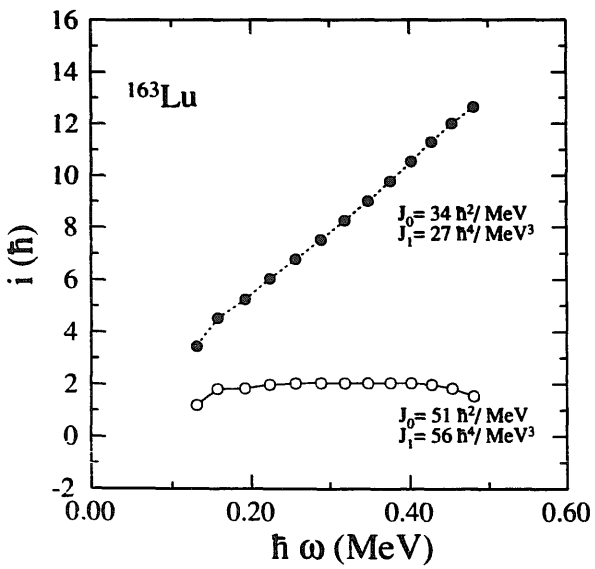

Fig. 12. Aligned angular momentum for the $[660]^{1+}_{\frac{1}{2}}$ band in ^{163}Lu. Two different sets of reference core parameters were used (see text).

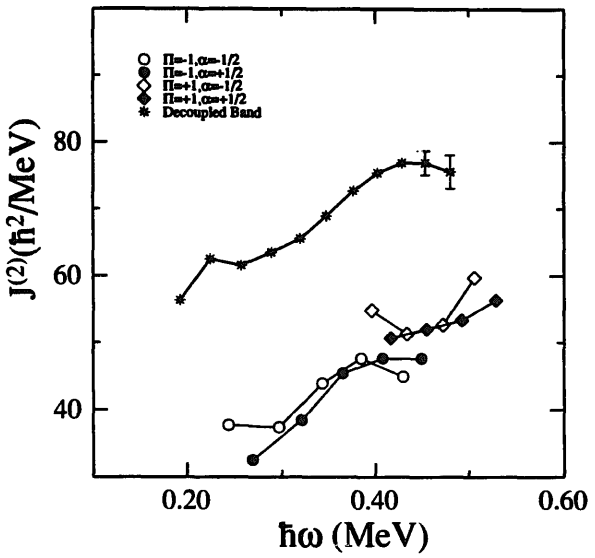

Fig. 13. Dynamic moments of inertia for the decoupled band and for the strongly coupled bands (outside the band crossing region) in ^{163}Lu.

and its value varies only slowly over the whole frequency range. This suggests a larger deformation and it is appropriate to use a different core of reference for that band. A fit of $J^{(2)} = J_0 + \frac{1}{3}\omega^2 J_1$ to the experimental data up to $\hbar\omega = 0.43$ MeV gives the Harris parameters $J_0 = 51\,\hbar^2/\text{MeV}$ and $J_1 = 56\,\hbar^4/\text{MeV}^3$ which are appreciably larger than those of the $[404]\frac{7}{2}^+$ and the $[514]\frac{9}{2}^-$ bands (see above). The alignment obtained with this reference is constant over the whole frequency range, see fig. 12 (open circles). There is also more direct evidence for a larger deformation of the decoupled band: in recent Doppler-shift lifetime experiments [24]) we find much shorter lifetimes of transitions in that band compared to the ones in the $[514]\frac{9}{2}^-$ strongly coupled band. A preliminary analysis gives transition quadrupole moments that are almost twice as large as the normal ones; but a more quantitative statement has to wait until a careful analysis of the data has been carried out [24]).

It is very puzzling that the decoupled band does not show any sign of band crossing up to the highest frequencies observed. If it would be the $[541]\frac{1}{2}^-$ band as suggested by Honkanen *et al.* [3]) a somewhat larger neutron crossing frequency than for the other bands would be expected. This Nilsson level is strongly downsloping with increasing deformation and has a prolate-driving effect on the nucleus. In fact, theoretical calculations [18]) of band-head deformations predict a deformation parameter $\beta_2 = 0.26$ for this state, as compared to values around $\beta_2 = 0.22$ for the other levels in ^{163}Lu. Our TRS calculations give $\beta_2 = 0.26$ also at higher frequencies (see lower left of fig. 10) for the $[541]\frac{1}{2}^-$ configuration. Caused by the larger deformation the neutron band crossing frequencies are lying systematically higher in the $[541]\frac{1}{2}^-$ configuration than in the less deformed bands in the same nuclei. This shift is up to 80 keV in this mass region [1]). Fig. 11 shows that the $i_{13/2}$ neutron alignment is expected below $\hbar\omega = 0.25$ MeV according to our CSM calculations and that it is

not possible to reproduce a crossing frequency of $\hbar\omega > 0.45$ MeV with a deformation parameter around 0.26. On the other hand, the experimentally observed crossing frequencies in $[541]\frac{1}{2}^-$ bands in the neighbouring isotopes are well within the range of the calculation.

This has led us to a search for bands in other nuclei with a similar behaviour. Indeed, in several Ta [ref. [9])], Re [refs. [13,14])] and Ir [refs. [16,20])] isotopes such bands have been observed previously. They were assigned as $[660]\frac{1}{2}^+$ $i_{13/2}$ proton configurations. The proton $i_{13/2}$ intruder level is even more prolate-driving than the $[541]\frac{1}{2}^-$ $h_{9/2}$ orbital. Our TRS calculations give a minimum at a very large deformation, $\beta_2 = 0.33$, for the $[660]\frac{1}{2}^+$ configuration (see lower right of fig. 10). We have calculated the single-particle proton energy levels at this deformation as a function of rotational frequency and indeed, the $[660]\frac{1}{2}^+$ $i_{13/2}$ proton intruder state lies close to the Fermi level. The situation is very similar to the $A = 135$ region, where the neutron $i_{13/2}$ $[660]\frac{1}{2}^+$ intruder bands have been identified in several odd-N nuclei [31-36]) and show a larger deformation of $\beta_2 = 0.3$-0.4. In these nuclei the $i_{13/2}$ neutron is the intruder and the expected proton alignments do not occur at all or with much larger than normal interaction strength. It was suggested [19]) that a strong residual proton-neutron interaction may be responsible for this effect. Thus, it might not be too surprising that in our case of ^{163}Lu we do not observe the neutron alignment in the $i_{13/2}$ proton intruder band.

The second decoupled band which is only weakly populated in ^{163}Lu shows an upbend at $\hbar\omega \simeq 0.3$ MeV. If this is caused by the alignment of an $i_{13/2}$ neutron pair, the crossing frequency is probably higher than that of the corresponding alignments in the strongly coupled bands, see table 3. A more moderate shift to higher frequency is consistent with that observed for $[541]\frac{1}{2}^-$ bands in neighbouring nuclei [1]). We suggest that this band may be based on the $[541]\frac{1}{2}^-$ configuration. We conjecture that the $[660]\frac{1}{2}^+$ band is populated more strongly than the $[541]\frac{1}{2}^-$ band in ^{163}Lu because it is closer to yrast at high spins due to its large moment of inertia.

5. Conclusions

High-spin states in ^{163}Lu were investigated by in-beam γ-ray spectroscopy using the multi-detector array OSIRIS. The level scheme was extended to much higher spins and an additional strongly coupled band was added. The most interesting result is that the decoupled band which has a much larger moment of inertia shows no sign of a band crossing up to the highest observed rotational frequency of 0.48 MeV. A re-interpretation of the configuration of this sequence (which was previously assigned as $[541]\frac{1}{2}^-$) as a $[660]\frac{1}{2}^+$ intruder band with large deformation is suggested.

The $i_{13/2}$ neutron band crossing is observed in the two strongly coupled bands which we assign as $[514]\frac{9}{2}^-$ and $[404]\frac{7}{2}^+$ proton configurations. A second band crossing which is only seen in the positive-parity coupled band is due to the alignment

of a $h_{11/2}$ proton pair. Comparison of calculated and experimental band-crossing frequencies, $B(M1)/B(E2)$ ratios and the signature splitting Δe indicate a sizeable γ-deformation for the $[514]^{9-}_{2}$ band below the band crossing. Together with the results of TRS calculations a consistent picture of coexistence of different shapes in ^{163}Lu is obtained.

The authors wish to thank Drs. G.B. Hagemann, R. Bengtsson and S. Frauendorf for helpful discussions. One of us (W.S.) wants to thank the Cusanuswerk for a fellowship and one of us (N.S.) wants to thank the Heinrich Hertz Foundation for financial support. A.P.B. gratefully acknowledges the support from the A.v. Humboldt Foundation. The work was supported financially by the Bundesminister für Forschung und Technologie BRD (contract No. 06BN181) and by the Minister für Wissenschaft und Forschung NRW, as well as by the US Department of Energy (contract No. DE-FG05-87ER40361)

References

1) C.-H. Yu, G.B. Hagemann, J.M. Espino, K. Furuno, J.D. Garrett, R. Chapman, D. Clarke, F. Khazaie, J.C. Lisle, J.N. Mo, M. Bergström, L. Carlén, P. Ekström, J. Lyttkens and H. Ryde, Nucl. Phys. **A511** (1990) 157
2) S. Jönsson, J. Lyttkens, L. Carlén, N. Roy, H. Ryde, W. Walús, J. Kownacki, G.B. Hagemann, B. Herskind, J.D. Garrett and P.O. Tjøm, Nucl. Phys. **A422** (1984) 397
3) K. Honkanen, H.C. Griffin, D.G. Sarantites, V. Abenante, L.A. Adler, C. Baktash, Y.S. Chen, O. Dietzsch, M.L. Halbert, D.C. Hensley, N.R. Johnson, A.J. Larabee, I.Y. Lee, L.L. Riedinger, J.X. Saladin, T.M. Semkow and Y. Schutz, ACS Symp. Series **324**, Nuclei off the line of stability, p. 317
4) C.-H. Yu, M.A. Riley, J.D. Garrett, G.B. Hagemann, J. Simpson, P.D. Forsyth, A.R. Mokhtar, J.D. Morrison, B.M. Nyakó, J.F. Sharpey-Schafer and R. Wyss, Nucl. Phys. **A489** (1988) 477
5) S. Ogaza, J. Gascon, H.J. Jensen, J. Nyberg, M.P. Carpenter, G.B. Hagemann, Y. Iwata, T. Komatsubara, G. Sletten and P.O. Tjøm, NBI preprint
6) G.B. Hagemann, B. Herskind, J. Kownacki, B.M. Nyakó, P.L. Nolan and J.F. Sharpey-Schafer, Nucl. Phys. **A424** (1984) 365
7) D.C. Radford, H.R. Andrews, D. Horn, D. Ward, F. Banville, S. Flibotte, P. Taras, J. Johannssen, D. Tucker and J.C. Waddington, Workshop on nuclear structure, NBI, Copenhagen, May 1988
8) A.J. Larabee, L.H. Courtney, S. Frauendorf, L.L. Riedinger, J.C. Waddington, M.P. Fewell, N.R. Johnson, I.Y. Lee and F.K. McGowan, Phys. Rev. **C29** (1984) 1934
9) C.X. Yang, J. Kownacki, J.D. Garrett, G.B. Hagemann, B. Herskind, J.C. Bacelar, J.R. Leslie, R. Chapman, J.C. Lisle, J.N. Mo, A. Simcock, J.C. Wilmott, W. Walús, L. Carlén, S. Jönsson, J. Lyttkens, H. Ryde, P.O. Tjøm and P.M. Walker, Phys. Lett. **B133** (1983) 39
10) J. Gascon, P. Taras, D.C. Radford, D. Ward, H.R. Andrews and F. Banville, Nucl. Phys. **A467** (1987) 539
11) A.G. Smith, R. Chapman, J. Copnell, S.J. Freeman, J. Irwin, F. Khazaie, J.C. Lisle, G.S. Li, J.N. Mo, C. Tenreiro, G.J. Yuan and G.B. Hagemann, Manchester University Nuclear Physics Annual Report, Jan. 1989-Dec. 1990, p. 86
12) J.C. Bacelar, R. Chapman, J.R. Leslie, J.C. Lisle, J.N. Mo, E. Paul, A. Simcock, J.C. Willmott, J.D. Garrett, G.B. Hagemann, B. Herskind, A. Holm and P.M. Walker, Nucl. Phys. **A442** (1985) 547
13) R.A. Bark, G.D. Dracoulis, A.E. Stuchbery, A.P. Byrne, A.M. Baxter, F. Riess and P.K. Weng, Nucl. Phys. **A501** (1989) 157
14) R.A. Bark, G.D. Dracoulis, A.E. Stuchbery, A.P. Byrne, A.M. Baxter, F. Riess and P.K. Weng, J. of Phys. **G15** (1989) L169

15) Ts. Venkova, T. Morek, R.M. Lieder, W. Gast, G. Hebbinghaus, A. Krämer-Flecken, W. Urban and K.H. Maier, Z. Phys. **A334** (1989) 385
16) S. Juutinen, P. Ahonen, J. Hattula, R. Julin, A. Pakkanen, A. Virtanen, J. Simpson, R. Chapman, D. Clarke, F. Khazaie, J.C. Lisle and J.N. Mo, preprint
17) V.P. Janzen, M.P. Carpenter, L.L. Riedinger, W. Schmitz, S. Pilotte, S. Monaro, D.D. Rajnauth, J.K. Johansson, D.G. Popescu, J.C. Waddington, Y.S. Chen, F. Doenau and P.B. Semmes, Phys. Rev. Lett. **61** (1988) 2073
18) W. Nazarewicz, M.A. Riley and J.D. Garrett, Nucl. Phys. **A512** (1990) 61
19) R. Wyss and A. Johnsson, Int. Conf. on high-spin-physics and gamma-soft nuclei, Pittsburgh (1990)
20) L.L. Riedinger, H.-Q. Jin and C.-H. Yu, Nucl. Phys. **A520** (1990) 287c
21) I. Hamamoto, Nucl. Phys. **A520** (1990) 297c
22) G.B. Hagemann, J. Gascon, C.-H. Yu, D.C. Radford and I. Hamamoto, Invited Talk at the XXIV Zakopane School on Physics 1989
23) U.J. Schrewe, E. Hagberg, H. Schmeing, J.C. Hardy, V.T. Koslowsky, K.S. Sharma and E.T.H. Clifford, Phys. Rev. **C25** (1982) 3091
24) W. Schmitz, C.X. Yang, G. Baldsiefen, U. Birkental, G. Fröhlingsdorf, H. Hübel, D. Mehta, R. Müsseler, M. Neffgen, P. Willsau, J. Gascon, G.B. Hagemann, A. Maj, D. Müller, J. Nyberg, M. Piiparinen and A. Virtanen, to be published
25) F. Dönau, Nucl. Phys. **A471** (1987) 469
26) R. Bengtsson and S. Frauendorf, Nucl. Phys. **A327** (1979) 139
27) J.D. Garrett, O. Andersen, J.J. Gaardhøje, G.B. Hagemann, B. Herskind, J. Kownacki, J.C. Lisle, L.L. Riedinger, W. Walús, N. Roy, S. Jönsson, H. Ryde, M. Guttormsen and P.O. Tjøm, Phys. Rev. Lett. **47** (1981) 75
28) W. Nazarewicz, J. Dudek, R. Bengtsson, T. Bengtsson and I. Ragnarsson, Nucl. Phys. **A435** (1985) 397
29) S. Cwiok, J. Dudek, W. Nazarewicz, J. Skalski and T. Werner, Comput. Phys. Comm. **46** (1987) 379
30) R. Wyss, to be published
31) R. Wyss, J. Nyberg, A. Johnson, R. Bengtsson and W. Nazarewicz, Phys. Lett. **B215** (1988) 211
32) R. Wadsworth, P. Regan, S.M. Mullins, G.J. Gyapong, D.L. Watson, P.J. Nolan, M.J. Godfrey, I. Jenkins, Y.J. He, B.J. Varley, W. Gelletly and J. Simpson, Z. Phys. **A333** (1989) 409
33) S.M. Mullins, R. Wadsworth, J.M. O'Donnell, P.J. Nolan, A.J. Kirwan, P.J. Bishop, M.J. Godfrey and D.J.G. Love, J. of Phys. **G13** (1987) L201
34) E.S. Paul, R. Ma, C.W. Beausang, D.B. Fossan, W.F. Piel Jr., S. Shi, N. Xu and J. Zhang, Phys. Lett. **61** (1988) 42
35) R. Ma, C.W. Beausang, E.S. Paul, W.F. Piel Jr, S. Shi, N. Xu, D.B. Fossan, J. Burde, M.A. Delaplanque, R.M. Diamond, A.O. Machiavelli and F.S. Stephens, Phys. Rev. **C40** (1989) 156
36) P.H. Regan, R. Wyss, R. Wadsworth, D.B. Fossan, Y.-J. He, J.R. Hughes, I. Jenkins, R. Ma, M.S. Metcalfe, S.M. Mullins, P.J. Nolan, E.S. Paul, R.J. Poynter and N. Xu, Phys. Rev. **C42** (1990) R1805